

See discussions, stats, and author profiles for this publication at:
<https://www.researchgate.net/publication/259095135>

A new numerical implementation of a second-gradient model for plastic porous solids, with an application of ductile rupture tests

ARTICLE *in* COMPUTER METHODS IN APPLIED MECHANICS AND ENGINEERING · JANUARY 2014

Impact Factor: 2.96 · DOI: 10.1016/j.cma.2013.09.006

CITATIONS

2

READS

114

3 AUTHORS:



Jean-Michel Bergheau

École nationale d'ingénieurs de Saint-...

362 PUBLICATIONS 1,448 CITATIONS

SEE PROFILE



Jean-Baptiste Leblond

Pierre and Marie Curie University - Pari...

172 PUBLICATIONS 3,826 CITATIONS

SEE PROFILE



Gilles Perrin

AREVA

29 PUBLICATIONS 1,215 CITATIONS

SEE PROFILE



A new numerical implementation of a second-gradient model for plastic porous solids, with an application to the simulation of ductile rupture tests



Jean-Michel Bergheau^a, Jean-Baptiste Leblond^{b,*}, Gilles Perrin^c

^a Université de Lyon, ENISE, LTDS, UMR 5513 CNRS, 58 rue Jean Parot, 42023 Saint-Etienne Cedex 02, France

^b UPMC Univ Paris 06, UMR 7190, Institut Jean Le Rond d'Alembert, Tour 65-55, 4 place Jussieu, 75005 Paris, France

^c AREVA, Tour Areva, 1 place Jean Millier, 92084 Paris La Défense Cedex, France

ARTICLE INFO

Article history:

Received 9 April 2013

Received in revised form 29 August 2013

Accepted 2 September 2013

Available online 25 September 2013

Keywords:

Ductile rupture

Second-gradient model

Numerical implementation

Simulation of rupture tests

ABSTRACT

An interesting second-gradient model for plastic porous solids, extending Gurson (1977)'s standard first-gradient model, was proposed by Gologanu et al. (1997) in order to settle the issue of unlimited localization of strain and damage and the ensuing mesh sensitivity in finite element calculations. Gologanu et al. (1997)'s model was implemented in a finite element code by Enakoutsa (2007), Enakoutsa and Leblond (2009). The implementation however rose two difficulties: (i) the number of degrees of freedom per node was awkwardly large because of the introduction of extra nodal degrees of freedom representing strains; (ii) convergence of the global elastoplastic iterations was often very difficult.

A new implementation solving these problems is presented in this work. An original procedure of elimination of the nodal degrees of freedom representing the strains permits to reduce the number of degrees of freedom per node to its standard value. Also, the convergence issue is solved through use of normally integrated linear elements instead of more customary subintegrated quadratic ones.

As an application, 2D numerical simulations of experiments of ductile rupture of a pre-notched and pre-cracked axisymmetric specimen and a CT specimen are performed. The calculations are pursued without difficulties up to a late stage of the rupture process, and the results are mesh-independent. Also, a good agreement between experimental and computed load–displacement curves is obtained for values of the parameters governing void coalescence compatible with those suggested by micromechanical numerical simulations, which could never be achieved in calculations based on Gurson (1977)'s standard model.

© 2013 Elsevier B.V. All rights reserved.

1. Introduction

Some years ago, Gologanu et al. [8] proposed a second-gradient model for plastic porous solids aimed at solving the problem of unlimited localization of strain and damage, resulting in mesh-dependent results in finite element calculations, encountered upon use of Gurson's [9] standard first-gradient model. Unlike alternative solutions of the problem (such as that of Leblond et al. [13], studied in detail by Enakoutsa et al. [4]), Gologanu et al.'s [8] model was not based on purely heuristic grounds but on some extension of Gurson's [9] approximate homogenization of a hollow sphere (typical elementary cell in a

* Corresponding author. Tel.: +33 144273924.

E-mail address: jbl@lmm.jussieu.fr (J.-B. Leblond).

porous medium) subjected to Hill-Mandel [14,10] – type conditions of homogeneous boundary strain rate. The novelty of Gologanu et al.'s [8] approach consisted in assuming the velocity to be a quadratic rather than linear function of the coordinates on the boundary of the cell; the physical idea being to approximately account in this way for possible quick variations of the macroscopic strain rate over short distances of the order of the void spacing. (The same idea was also proposed independently, almost simultaneously, by Forest [7]).

Gologanu et al.'s [8] model was implemented into ESI Group's SYSTUS® finite element code by Enakoutsa [3], Enakoutsa and Leblond [5]. The model was found to have important potential in that (i) numerical results were checked to be essentially mesh-independent, as hoped; and (ii) experiments of ductile rupture of typical specimens could be simulated satisfactorily for some suitable choice of the model parameters.

The numerical implementation of Enakoutsa [3], Enakoutsa and Leblond [5] was however hampered by two severe difficulties:

- The introduction of extra nodal degrees of freedom (DOF) representing strains, aimed at permitting the calculation of the spatial derivatives of these strains, increased the number of DOF per node from 2 to 6 in 2D, and from 3 to 9 in 3D. This made the calculations very heavy.
- Convergence of the global elastoplastic iterations was often very problematic, even when a consistent tangent matrix was used. As a result, for some problems, results could be obtained only by adopting a basically unreliable *explicit* algorithm with respect to the plastic strain rate; that is, by calculating the plastically corrected stresses at the end of each time interval using the plastic strain rate corresponding to the *preceding* interval.

The aim of the present work is to propose an innovative algorithm solving these difficulties, with some new significant applications.

It is worth noting here that the first difficulty in fact arises for *all* second-gradient models, and that similarly the solution proposed to it in this paper potentially applies to all such models.¹ (In contrast, the second difficulty is more specific to the particular model considered since it arises from its softening character; and so is also the associated remedy).

It is clear that the difficulties encountered in Enakoutsa's [3], Enakoutsa and Leblond's [5] implementation of Gologanu et al.'s [8] model arose at least partly from a common central point of all implementations of second-gradient models, namely the evaluation of spatial derivatives of the strains. The method adopted by Enakoutsa [3], Enakoutsa and Leblond [5] and Fernandes et al. [6] consisted in (i) deducing these derivatives from the newly introduced nodal DOF representing strains using the first derivatives of the shape functions, and (ii) enforcing the approximate coincidence of these new DOF and the strains through some penalty method. The drawbacks of such an approach are well-known: the number of DOF per node becomes awkwardly large, and care must be taken to select the penalty coefficient which must be sufficiently large to be effective, but not too much in order not to generate an ill-conditioned tangent matrix. An alternative approach, used by Shu et al. [18] and Matsushima et al. [16,17] consists in using the method of Lagrange multipliers to enforce coincidence of the new nodal DOF and the strains. But this method increases the number of DOF even more, and generates an additional risk of ill-conditioning of the tangent matrix since the set of unknowns consists of quantities of distinct dimensions. Still another option, used by Chambon et al. [2] for 1D problems and Zervos et al. [23] for 2D ones, consists of using elements of class C^1 ; but such elements are very cumbersome in 2D and 3D and as a rule not available in standard codes.

We shall therefore adopt here a new approach to calculate the derivatives of the strains. This approach consists in retaining the introduction of new nodal DOF representing strains, but writing the equality of these DOF and the strains in a weak sense. The left-hand side of the vectorial relation connecting the new DOF to the nodal displacements then involves a "mass matrix" analogous to that encountered in dynamic problems. Following the usual procedure for such problems (see e.g. Hughes [11]), one may lump this matrix, invert it straightforwardly, and express the new DOF explicitly in terms of the displacements, so as to eliminate them. In this way the unknowns are reduced to the sole displacements, like for a standard first-gradient model, and there is no risk of an ill-conditioned tangent matrix.

In addition, the model will be implemented not only with subintegrated quadratic elements, as customarily employed in plasticity, but also with normally integrated linear elements. No locking problem will arise from use of a standard integration scheme since materials obeying Gologanu et al.'s [8] model, being porous, are plastically compressible; and elimination of nodes located half-way along the element edges will prove essential to improve the convergence of the elastoplastic iterations.

The paper is organized as follows:

- Section 2 provides a brief but complete presentation of Gologanu et al.'s [8] second-gradient model.
- Section 3 describes the new numerical implementation proposed, with special emphasis on the procedure of calculation and elimination of the extra nodal DOF representing strains.
- Section 4 presents a validation of the programme based on the numerical solution of a problem of circular bending of a beam in plane strain, for which a reference analytical solution is available for some special values of the model parameters (Enakoutsa [3], Enakoutsa and Leblond [5]).

¹ It does *not* apply, however, to "micropolar" or "micromorphic" models involving extra kinematic variables independent of the second-gradient of the displacement.

- Finally Section 5 presents some applications, in the form of 2D numerical simulations of two typical experiments of ductile rupture, performed on a pre-notched and pre-cracked axisymmetric specimen and a CT specimen made of different materials.

2. Second-gradient model for porous plastic solids

The original reference of Gologanu et al.'s [8] model is not easily accessible, but a complete presentation of its equations has been given by Enakoutsu and Leblond [5], together with a summary of the underlying homogenization procedure. Their presentation is summarized here for ease of reference and to make the paper self-contained.

2.1. Description of internal forces – virtual powers of internal and external forces

Gologanu et al.'s [8] model is formulated within a Eulerian setting involving large displacements and strains. Internal forces are represented through Cauchy's usual stress tensor $\boldsymbol{\sigma}$ plus some third-rank "moment tensor" \mathbf{m} symmetric in its first two indices only. The components of \mathbf{m} are related through the conditions

$$m_{ijj} = 0. \quad (1)$$

(These relations basically arise from the fact that the mechanical quantities m_{ijj} are "conjugate" to kinematic quantities which represent rigid-body motions of the elementary spherical hollow cell considered in the micromechanical derivation of the model; see Appendix A of Enakoutsu and Leblond [5]).

The virtual power of internal forces $\mathcal{P}^{(i)}$ is given by

$$\mathcal{P}^{(i)} \equiv - \int_{\Omega} \left[\boldsymbol{\sigma}(\mathbf{x}) : \mathbf{d}^*(\mathbf{x}) + \mathbf{m}(\mathbf{x}) : \nabla \mathbf{d}^*(\mathbf{x}) \right] d\Omega. \quad (2)$$

In this expression Ω denotes the domain considered, \mathbf{x} the current position-vector, $\mathbf{d}^*(\mathbf{x}) \equiv \frac{1}{2} [(\nabla \mathbf{v}^*)(\mathbf{x}) + (\nabla \mathbf{v}^*)^T(\mathbf{x})]$ the Eulerian strain rate associated to the virtual velocity field $\mathbf{v}^*(\mathbf{x})$, and the symbols: and $:$ the double and triple inner products ($\boldsymbol{\sigma} : \mathbf{d}^* \equiv \sigma_{ij} d_{ij}^*$, $\mathbf{m} : \nabla \mathbf{d}^* \equiv m_{ijk} \partial d_{ij}^* / \partial x_k$).

The virtual power of external forces $\mathcal{P}^{(e)}$ is given, assuming absence of body loads, by

$$\mathcal{P}^{(e)} \equiv \int_{\partial\Omega} \mathbf{T}(\mathbf{u}(\mathbf{x})) \cdot \mathbf{v}^*(\mathbf{x}) dS \quad (3)$$

where \mathbf{T} represents some surface traction. This traction is considered to be a given function of the displacement \mathbf{u} ; this covers all classical types of boundary conditions: (i) the case of a prescribed traction (when \mathbf{T} is independent of \mathbf{u}); (ii) that of an elastic connection to some external body (when \mathbf{T} is a linear-affine function of \mathbf{u}); and (iii) that of a prescribed displacement (when the coefficient of this linear-affine function is large).

In theory, for such a second-gradient model, the integrand of the expression (3) of $\mathcal{P}^{(e)}$ should include some extra term proportional to \mathbf{d}^* . The reason for *not* including such a term was explained as follows by Gologanu et al. [8]: *One could imagine adding some term proportional to $\nabla \mathbf{v}^*$ to the integrand; the cofactor of that quantity would represent a "surface moment". This would make sense, however, only if there were significant variations of the microscopic surface traction over elementary cells, i.e. over distances of the order of the void spacing. We suppose that such is not the case here, because strong gradients of macroscopic fields arise from the softening character of the material (due to the porosity), not from some pathological character of the boundary conditions.* We shall follow Gologanu et al. [8] here but nevertheless explain in Section 3.5 below how such an additional term in the expression of $\mathcal{P}^{(e)}$ (which is generally necessary in second-gradient models) could be accounted for in the numerical implementation proposed.

2.2. Decomposition of the strain rate

The hypothesis of additive decomposition of the strain rate into elastic and plastic parts, extended in a natural way to its gradient, reads

$$\begin{cases} \mathbf{d} & \equiv \mathbf{d}^e + \mathbf{d}^p \\ \nabla \mathbf{d} & \equiv (\nabla \mathbf{d})^e + (\nabla \mathbf{d})^p, \end{cases} \quad (4)$$

where the elastic and plastic parts $(\nabla \mathbf{d})^e$, $(\nabla \mathbf{d})^p$ of the gradient of the strain rate do not coincide in general with the gradients $\nabla(\mathbf{d}^e)$, $\nabla(\mathbf{d}^p)$ of the elastic and plastic parts of this strain rate.

2.3. Hypoelasticity law

The elastic parts of the strain rate and its gradient are related to the rates of the stress and moment tensors through the following hypoelasticity laws:

$$\begin{cases} \frac{D\sigma_{ij}}{Dt} = \lambda \delta_{ij} d_{kk}^e + 2\mu d_{ij}^e \\ \frac{Dm_{ijk}}{Dt} = \frac{b^2}{5} \left[\lambda \delta_{ij} (\nabla d)_{hhk}^e + 2\mu (\nabla d)_{ijk}^e - 2\lambda \delta_{ij} U_k^e - 2\mu (\delta_{ik} U_j^e + \delta_{jk} U_i^e) \right]. \end{cases} \quad (5)$$

In these expressions,

- λ and μ denote the Lamé coefficients;
- b represents a “microstructural distance” of the order of the mean half-spacing between neighboring voids (in Gologanu et al.’s [8] micromechanical derivation of the model, it was the radius of the elementary spherical hollow cell considered);
- $D\sigma_{ij}/Dt$ and Dm_{ijk}/Dt are the Jaumann (objective) time-derivatives of σ_{ij} and m_{ijk} , given by

$$\begin{cases} \frac{D\sigma_{ij}}{Dt} & \equiv \dot{\sigma}_{ij} + \omega_{ki} \sigma_{kj} + \omega_{kj} \sigma_{ik} \\ \frac{Dm_{ijk}}{Dt} & \equiv \dot{m}_{ijk} + \omega_{hi} m_{hjk} + \omega_{hj} m_{ihk} + \omega_{hk} m_{ijh} \end{cases} \quad (6)$$

where the ω_{ij} are the components of the antisymmetric part $\boldsymbol{\omega} \equiv \frac{1}{2} [\nabla \mathbf{v} - (\nabla \mathbf{v})^T]$ of the velocity gradient;

- finally \mathbf{U}^e is a vector whose value is fixed by Eq. (1) written in rate form, $\frac{Dm_{ijk}}{Dt} = 0$:

$$U_i^e = \frac{\lambda (\nabla d)_{hhi}^e + 2\mu (\nabla d)_{ihh}^e}{2\lambda + 8\mu}. \quad (7)$$

2.4. Yield criterion

The plastic behavior is governed by the following “extended Gurson criterion”:

$$\Phi(\boldsymbol{\sigma}, \mathbf{m}, p, \bar{\sigma}) \equiv \frac{1}{\bar{\sigma}^2} \left(\sigma_{eq}^2 + \frac{Q^2}{b^2} \right) + 2p \cosh \left(\frac{3}{2} \frac{\sigma_m}{\bar{\sigma}} \right) - 1 - p^2 \leq 0. \quad (8)$$

In this expression,

- $\sigma_{eq} \equiv (\frac{3}{2} \boldsymbol{\sigma}' : \boldsymbol{\sigma}')^{1/2}$ ($\boldsymbol{\sigma}'$: deviator of $\boldsymbol{\sigma}$) denotes the von Mises equivalent stress;
- $\sigma_m \equiv \frac{1}{3} \text{tr} \boldsymbol{\sigma}$ denotes the mean stress;
- p is a parameter connected to the porosity (void volume fraction) f through the relation

$$p \equiv qf^*, \quad f^* \equiv \begin{cases} f & \text{if } f \leq f_c \\ f_c + \delta(f - f_c) & \text{if } f > f_c \end{cases} \quad (9)$$

where q is Tvergaard’s parameter [19], f_c the critical porosity at the onset of void coalescence and $\delta (> 1)$ a factor describing the accelerated degradation of the material during this coalescence Tvergaard and Needleman [20];

- $\bar{\sigma}$ represents some “average yield stress” of the heterogeneous voided matrix, the evolution of which is presented below;
- Q^2 is a quadratic form of the components of \mathbf{m} given by

$$Q^2 \equiv A_I m_I + A_{II} m_{II}, \quad \begin{cases} A_I & = 0.194 \\ A_{II} & = 6.108 \end{cases} \quad (10)$$

where m_I and m_{II} are the quadratic invariants of \mathbf{m} defined by:

$$\begin{cases} m_I & \equiv \frac{1}{9} m_{iik} m_{jjk} \\ m_{II} & \equiv \frac{3}{2} m'_{ijk} m'_{ijk}, \end{cases} \quad (11)$$

$m'_{ijk} \equiv m_{ijk} - \frac{1}{3} m_{hhk} \delta_{ij}$ denoting the components of the deviatoric part of \mathbf{m} , taken over its first two indices;

- and b is the same microstructural distance as above.

2.5. Flow rule

The plastic parts of the strain rate and its gradient are given by the flow rule associated to the criterion (8) through the normality property:

$$\begin{cases} d_{ij}^p = \eta \frac{\partial \Phi}{\partial \sigma_{ij}}(\boldsymbol{\sigma}, \mathbf{m}, p, \bar{\sigma}) \\ (\nabla d)_{ijk}^p = \eta \frac{\partial \Phi}{\partial m_{ijk}}(\boldsymbol{\sigma}, \mathbf{m}, p, \bar{\sigma}) + \delta_{ik} U_j^p + \delta_{jk} U_i^p, \end{cases} \quad \eta \begin{cases} = 0 & \text{if } \Phi(\boldsymbol{\sigma}, \mathbf{m}, p, \bar{\sigma}) < 0 \\ \geq 0 & \text{if } \Phi(\boldsymbol{\sigma}, \mathbf{m}, p, \bar{\sigma}) = 0. \end{cases} \quad (12)$$

The term $\delta_{ik} U_j^p + \delta_{jk} U_i^p$ in Eq. (12)₂ represents an arbitrary rigid-body motion of the elementary cell left unspecified by the flow rule, but fixed in practice by conditions (1).

2.6. Evolution of internal parameters

The evolution of the porosity f is governed by the classical equation

$$\dot{f} = (1 - f) \operatorname{tr} \mathbf{d}^p \quad (13)$$

resulting from approximate incompressibility of the metallic matrix. Also, the parameter $\bar{\sigma}$ is given by

$$\bar{\sigma} \equiv \sigma(\bar{\epsilon}) \quad (14)$$

where $\sigma(\epsilon)$ denotes the yield stress of the sound material, depending on the equivalent cumulated plastic strain ϵ , and $\bar{\epsilon}$ is an “average equivalent strain” of the heterogeneous matrix. The evolution of this average strain is governed by the following equation, which stands as a natural extension of that proposed by Gurson [9]:

$$(1 - f) \sigma \dot{\bar{\epsilon}} = \boldsymbol{\sigma} : \mathbf{d}^p + \mathbf{m} : (\nabla \mathbf{d})^p. \quad (15)$$

2.7. Case of a zero porosity

Gologanu et al.'s [8] model was not defined with the case of a zero porosity in view, since these authors' aim was, in their own words, *to derive an approximate model for ductile porous solids including the effect of possible notable gradients of macroscopic mechanical fields at the scale of the void spacing (arising from the tendency of damage to localize)*. It may however be envisaged as a limit-case.

In the absence of voids, one would expect Gologanu et al.'s [8] model to reduce to the standard first-gradient model for a von Mises material. It is however clear that Gologanu et al.'s [8] criterion (8) does *not* reduce to that of von Mises in the limit $f \rightarrow 0$, because of the presence of the term $Q^2/(\bar{\sigma}^2 b^2)$ in the expression of the yield function $\Phi(\boldsymbol{\sigma}, \mathbf{m}, p, \bar{\sigma})$.

The issue is connected to the question of the choice of the value of the microstructural distance b in the absence of voids. In a porous material, b is unambiguously defined as the radius of the elementary spherical hollow cell to be considered in the micromechanical approach, of the order of the mean half-spacing between voids. In a sound material, however, the size of the elementary cell cannot be defined by non-existing voids, so that the only logical choice for it is $b \rightarrow 0$. In this limit the term $Q^2/(\bar{\sigma}^2 b^2)$ in the expression (8) of the yield function $\Phi(\boldsymbol{\sigma}, \mathbf{m}, p, \bar{\sigma})$ disappears (because Q^2 is of order b^4 by Eq. (5)₂); the criterion (8) then reduces to that of von Mises, as desired.

The conclusion is that *for vanishingly small values of the porosity, Gologanu et al.'s [8] model must logically be used with a vanishingly small value of the microstructural distance also*.

3. Numerical implementation

One central feature of the numerical implementation is of course the operation of “projection of the elastic predictor onto the yield locus” (plastic correction of the elastically computed stresses and moments). We shall not however insist on this aspect which has been described in detail by Enakoutsa and Leblond [5], and concentrate on novel features connected to the elimination of nodal variables representing strains. For conciseness, the presentation is given for 3D problems only; the extension to 2D or axisymmetric ones does not raise any particular difficulty. Of course, no simplifying assumptions are made concerning the magnitude of the displacements and strains.

3.1. Nodal variables and associated gradients

The displacement \mathbf{u} , its increment $\Delta \mathbf{u}$ between successive instants, and its virtual infinitesimal variation $\delta \mathbf{u}^*$ are interpolated using their values \mathbf{u}_p , $\Delta \mathbf{u}_p$, $\delta \mathbf{u}_p^*$ on a set of M nodes numbered with an index p , and the associated shape functions $N_p^u(\mathbf{x})$:

$$\mathbf{u}(\mathbf{x}) = N_p^u(\mathbf{x}) \mathbf{u}_p; \quad \Delta \mathbf{u}(\mathbf{x}) = N_p^u(\mathbf{x}) \Delta \mathbf{u}_p; \quad \delta \mathbf{u}^*(\mathbf{x}) = N_p^u(\mathbf{x}) \delta \mathbf{u}_p^* \quad (16)$$

where Einstein's summation convention is used for the index p .

We also introduce an extra tensorial variable $\Delta \mathbf{w}$, represented as a 6-vector $(\Delta w_\alpha)_{1 \leq \alpha \leq 6}$ using Voigt's notation, intended to represent the *strain increment* between successive instants,² and its virtual infinitesimal variation $\delta(\Delta \mathbf{w}^*) \equiv [\delta(\Delta w_\alpha^*)]_{1 \leq \alpha \leq 6}$. These variables are interpolated using their values $\Delta \mathbf{w}_q$, $\delta(\Delta \mathbf{w}_q^*)$ on a subset of N ($\leq M$) nodes numbered with an index q , and the associated shape functions $N_q^w(\mathbf{x})$:

$$\Delta \mathbf{w}(\mathbf{x}) = N_q^w(\mathbf{x}) \Delta \mathbf{w}_q; \quad \delta(\Delta \mathbf{w}^*)(\mathbf{x}) = N_q^w(\mathbf{x}) \delta(\Delta \mathbf{w}_q^*). \quad (17)$$

The shape functions $N_p^u(\mathbf{x})$ and $N_q^w(\mathbf{x})$ need not necessarily be identical. In fact, we shall consider two interpolation schemes:

- One based on a quadratic interpolation of \mathbf{u} -type variables and a linear interpolation of \mathbf{w} -type ones; in this case nodes located half-way along the element edges will be used to interpolate the former variables but not the latter.

² There will be no need to consider the *strain* itself.

- Another based on identical linear interpolations of \mathbf{u} - and \mathbf{w} -type variables; in that case the same set of nodes will be used to interpolate both types of variables.

Grouping the indices p and i representing node numbers and directions of space, we shall consider the $3M$ -vector \mathbf{U} of nodal displacements, of components $(u_{pi})_{1 \leq p \leq M, 1 \leq i \leq 3}$, together with its increment $\Delta \mathbf{U}$ between successive instants and its virtual infinitesimal variation $\delta \mathbf{U}^*$. Similarly, grouping the indices q and α , we shall consider the $6N$ -vector $\Delta \mathbf{W}$ of nodal values of the variable $\Delta \mathbf{w}$, of components $(\Delta w_{q\alpha})_{1 \leq q \leq N, 1 \leq \alpha \leq 6}$, together with its virtual infinitesimal variation $\delta(\Delta \mathbf{W}^*)$.

The small strain increment $\Delta \mathbf{e}(\mathbf{x}) \equiv \frac{1}{2} [\nabla(\Delta \mathbf{u})(\mathbf{x}) + (\nabla(\Delta \mathbf{u}))^T(\mathbf{x})]$ between successive instants, and its virtual infinitesimal variation $\delta \mathbf{e}^*(\mathbf{x}) \equiv \frac{1}{2} [\nabla(\delta \mathbf{u}^*)(\mathbf{x}) + (\nabla(\delta \mathbf{u}^*))^T(\mathbf{x})]$, may be calculated by differentiating Eqs. (16)_{2,3} with respect to the components of the position-vector \mathbf{x} in the current configuration. Representing these tensors as 6-vectors $(\Delta e_\alpha)_{1 \leq \alpha \leq 6}, (\delta e_\alpha^*)_{1 \leq \alpha \leq 6}$ using Voigt's notation, one gets

$$\Delta \mathbf{e}(\mathbf{x}) \equiv \mathbf{B}^u(\mathbf{x}) \cdot \Delta \mathbf{U}; \quad \delta \mathbf{e}^*(\mathbf{x}) \equiv \mathbf{B}^u(\mathbf{x}) \cdot \delta \mathbf{U}^* \quad (18)$$

where $\mathbf{B}^u(\mathbf{x})$ is a $6 \times 3M$ matrix involving the derivatives of the shape functions $N_p^u(\mathbf{x})$ in the current configuration. The gradients $\nabla(\Delta \mathbf{w})(\mathbf{x}), \nabla[\delta(\Delta \mathbf{w}^*)](\mathbf{x})$ of the increment $\Delta \mathbf{w}(\mathbf{x})$ and its infinitesimal variation $\delta(\Delta \mathbf{w}^*)(\mathbf{x})$ may similarly be obtained by differentiating Eqs. (17) with respect to the components of \mathbf{x} . Grouping again indices so as to represent these tensors as 18-vectors $(\partial \Delta w_\alpha / \partial x_i)_{1 \leq \alpha \leq 6, 1 \leq i \leq 3}, (\partial \delta(\Delta w_\alpha^*) / \partial x_i)_{1 \leq \alpha \leq 6, 1 \leq i \leq 3}$, one gets

$$\nabla(\Delta \mathbf{w})(\mathbf{x}) \equiv \mathbf{B}^w(\mathbf{x}) \cdot \Delta \mathbf{W}; \quad \nabla[\delta(\Delta \mathbf{w}^*)](\mathbf{x}) \equiv \mathbf{B}^w(\mathbf{x}) \cdot \delta(\Delta \mathbf{W}^*) \quad (19)$$

where $\mathbf{B}^w(\mathbf{x})$ is a $18 \times 6N$ matrix involving the derivatives of the shape functions $N_q^w(\mathbf{x})$ in the current configuration.

3.2. Elementary virtual works of internal and external forces

Using again Voigt's notation and grouping indices so as to represent the stress and moment tensors $\boldsymbol{\sigma}, \mathbf{m}$ as a 6-vector $(\sigma_\alpha)_{1 \leq \alpha \leq 6}$ and a 18-vector $(m_{\alpha i})_{1 \leq \alpha \leq 6, 1 \leq i \leq 3}$ respectively, one may express the elementary virtual work of internal forces $\delta \mathcal{W}_i^*$, by Eqs. (2), (18)₂ and (19)₂, in the form

$$\begin{aligned} \delta \mathcal{W}_i^* &\equiv - \int_{\Omega} \{ \boldsymbol{\sigma}(\mathbf{x}) \cdot \delta \mathbf{e}^*(\mathbf{x}) + \mathbf{m}(\mathbf{x}) \cdot \nabla[\delta(\Delta \mathbf{w}^*)](\mathbf{x}) \} d\Omega \\ &= - \int_{\Omega} [\boldsymbol{\sigma}(\mathbf{x}) \cdot \mathbf{B}^u(\mathbf{x}) \cdot \delta \mathbf{U}^* + \mathbf{m}(\mathbf{x}) \cdot \mathbf{B}^w(\mathbf{x}) \cdot \delta(\Delta \mathbf{W}^*)] d\Omega \end{aligned}$$

or equivalently

$$\delta \mathcal{W}_i^* = - \left(\int_{\Omega} [\mathbf{B}^u(\mathbf{x})]^T \cdot \boldsymbol{\sigma}(\mathbf{x}) d\Omega \right) \cdot \delta \mathbf{U}^* - \left(\int_{\Omega} [\mathbf{B}^w(\mathbf{x})]^T \cdot \mathbf{m}(\mathbf{x}) d\Omega \right) \cdot \delta(\Delta \mathbf{W}^*). \quad (20)$$

Also, rewriting Eq. (16) in the form

$$\mathbf{u}(\mathbf{x}) \equiv \mathbf{N}^u(\mathbf{x}) \cdot \mathbf{U}; \quad \Delta \mathbf{u}(\mathbf{x}) \equiv \mathbf{N}^u(\mathbf{x}) \cdot \Delta \mathbf{U}; \quad \delta \mathbf{u}^*(\mathbf{x}) \equiv \mathbf{N}^u(\mathbf{x}) \cdot \delta \mathbf{U}^* \quad (21)$$

where $\mathbf{N}^u(\mathbf{x})$ is a $3 \times 3M$ matrix involving the shape functions $N_p^u(\mathbf{x})$, one may express the elementary virtual work of external forces $\delta \mathcal{W}_e^*$, by Eq. (3), in the form

$$\delta \mathcal{W}_e^* \equiv \int_{\partial \Omega} \mathbf{T}(\mathbf{u}(\mathbf{x})) \cdot \delta \mathbf{u}^*(\mathbf{x}) dS = \int_{\partial \Omega} \mathbf{T}(\mathbf{u}(\mathbf{x})) \cdot \mathbf{N}^u(\mathbf{x}) \cdot \delta \mathbf{U}^* dS$$

or equivalently

$$\delta \mathcal{W}_e^* = \left(\int_{\partial \Omega} [\mathbf{N}^u(\mathbf{x})]^T \cdot \mathbf{T}(\mathbf{u}(\mathbf{x})) dS \right) \cdot \delta \mathbf{U}^*. \quad (22)$$

It follows from Eqs. (20) and (22) that

$$\delta \mathcal{W}_i^* + \delta \mathcal{W}_e^* \equiv -\mathbf{R}^u \cdot \delta \mathbf{U}^* - \mathbf{R}^w \cdot \delta(\Delta \mathbf{W}^*) \quad (23)$$

where the “partial residues” \mathbf{R}^u and \mathbf{R}^w are defined by

$$\begin{cases} \mathbf{R}^u &\equiv \int_{\Omega} [\mathbf{B}^u(\mathbf{x})]^T \cdot \boldsymbol{\sigma}(\mathbf{x}) d\Omega - \int_{\partial \Omega} [\mathbf{N}^u(\mathbf{x})]^T \cdot \mathbf{T}(\mathbf{u}(\mathbf{x})) dS \\ \mathbf{R}^w &\equiv \int_{\Omega} [\mathbf{B}^w(\mathbf{x})]^T \cdot \mathbf{m}(\mathbf{x}) d\Omega. \end{cases} \quad (24)$$

3.3. Expression of nodal strains in terms of nodal displacements

In order to enforce the approximate coincidence of the variable $\Delta \mathbf{w}$ and the increment of strain $\Delta \mathbf{e}$, we write the equality $\Delta \mathbf{w} = \Delta \mathbf{e}$ in a weak sense using the shape functions $N_q^w(\mathbf{x})$:

$$\int_{\Omega} N_q^w(\mathbf{x}) \Delta \mathbf{w}(\mathbf{x}) d\Omega = \int_{\Omega} N_q^w(\mathbf{x}) \Delta \mathbf{e}(\mathbf{x}) d\Omega,$$

that is, using Eqs. (17)₁ and (18)₁:

$$\int_{\Omega} N_q^w(\mathbf{x}) N_{q'}^w(\mathbf{x}) \Delta \mathbf{w}_{q'} d\Omega = \int_{\Omega} N_q^w(\mathbf{x}) \mathbf{B}^u(\mathbf{x}) \cdot \Delta \mathbf{U} d\Omega. \quad (25)$$

The left-hand side involves the matrix of components $\left(\int_{\Omega} N_q^w(\mathbf{x}) N_{q'}^w(\mathbf{x}) d\Omega \right)_{1 \leq q \leq N, 1 \leq q' \leq N}$, which is analogous to mass matrices encountered in dynamic problems and may therefore be lumped, following the usual procedure for such problems (Hughes, [11]). This operation is equivalent to simplifying Eq. (25) by assuming $\Delta \mathbf{w}_{q'} \simeq \Delta \mathbf{w}_q$ for those q' for which $\int_{\Omega} N_q^w(\mathbf{x}) N_{q'}^w(\mathbf{x}) d\Omega \neq 0$, which is reasonable for sufficiently refined meshes.

Since $\sum_{q'=1}^N N_{q'}^w(\mathbf{x}) = 1$ for every \mathbf{x} , the matrix is thus transformed into a diagonal one of (q, q) -component $\int_{\Omega} N_q^w(\mathbf{x}) d\Omega$, so that Eq. (25) may easily be solved to yield

$$\Delta \mathbf{w}_q = \frac{\int_{\Omega} N_q^w(\mathbf{x}) \mathbf{B}^u(\mathbf{x}) d\Omega}{\int_{\Omega} N_q^w(\mathbf{x}) d\Omega} \cdot \Delta \mathbf{U} \quad (\text{no sum on } q), \quad (26)$$

that is

$$\Delta \mathbf{W} = \mathbf{M} \cdot \Delta \mathbf{U} \quad (27)$$

where \mathbf{M} is a $6N \times 3M$ matrix. Also, by a similar reasoning,

$$\delta(\Delta \mathbf{W}^*) = \mathbf{M} \cdot \delta \mathbf{U}^*. \quad (28)$$

3.4. Elimination of nodal strains

The right-hand side of Eq. (23) must be equated to zero for all vectors $\delta \mathbf{U}^*$ and $\delta(\Delta \mathbf{W}^*)$ satisfying Eq. (28); this leads to

$$\mathbf{R}^u \cdot \delta \mathbf{U}^* + \mathbf{R}^w \cdot \mathbf{M} \cdot \delta \mathbf{U}^* = (\mathbf{R}^u + \mathbf{M}^T \cdot \mathbf{R}^w) \cdot \delta \mathbf{U}^* = 0 \quad \text{for all } \delta \mathbf{U}^*,$$

which implies that

$$\mathbf{R} \equiv \mathbf{R}^u + \mathbf{M}^T \cdot \mathbf{R}^w = \mathbf{0}. \quad (29)$$

In this equation the “partial residues” \mathbf{R}^u , \mathbf{R}^w , and consequently the “total residue” \mathbf{R} , are functions of the increments $\Delta \mathbf{U}$ and $\Delta \mathbf{W}$ and therefore, by Eq. (27), of the sole increment $\Delta \mathbf{U}$; and Eq. (29) must be solved with respect to this sole variable.

The matrix \mathbf{M} slightly depends upon $\Delta \mathbf{U}$ because of the presence, in the right-hand side of Eq. (26), of the matrix $\mathbf{B}^u(\mathbf{x})$ and thus of the gradients of the shape functions $N_p^u(\mathbf{x})$ in the current configuration. Neglecting this dependence,³ one may calculate the tangent matrix associated to Eq. (29):

$$\mathbf{K} \equiv \frac{\partial \mathbf{R}}{\partial \Delta \mathbf{U}} = \frac{\partial \mathbf{R}^u}{\partial \Delta \mathbf{U}} + \frac{\partial \mathbf{R}^u}{\partial \Delta \mathbf{W}} \cdot \frac{\partial \Delta \mathbf{W}}{\partial \Delta \mathbf{U}} + \mathbf{M}^T \cdot \left(\frac{\partial \mathbf{R}^w}{\partial \Delta \mathbf{U}} + \frac{\partial \mathbf{R}^w}{\partial \Delta \mathbf{W}} \cdot \frac{\partial \Delta \mathbf{W}}{\partial \Delta \mathbf{U}} \right),$$

that is, by Eq. (27):

$$\mathbf{K} \equiv \mathbf{K}^{uu} + \mathbf{K}^{uw} \cdot \mathbf{M} + \mathbf{M}^T \cdot \mathbf{K}^{wu} + \mathbf{M}^T \cdot \mathbf{K}^{ww} \cdot \mathbf{M}, \quad (30)$$

$$\begin{cases} \mathbf{K}^{uu} & \equiv \frac{\partial \mathbf{R}^u}{\partial \Delta \mathbf{U}} = \int_{\Omega} [\mathbf{B}^u(\mathbf{x})]^T \cdot \frac{\partial \boldsymbol{\sigma}}{\partial \Delta \mathbf{e}}(\mathbf{x}) \cdot \mathbf{B}^u(\mathbf{x}) d\Omega \\ & \quad - \int_{\partial \Omega} [\mathbf{N}^u(\mathbf{x})]^T \cdot \frac{\partial \boldsymbol{\pi}}{\partial \mathbf{u}}(\mathbf{x}) \cdot \mathbf{N}^u(\mathbf{x}) dS \\ \mathbf{K}^{uw} & \equiv \frac{\partial \mathbf{R}^u}{\partial \Delta \mathbf{W}} = \int_{\Omega} [\mathbf{B}^u(\mathbf{x})]^T \cdot \frac{\partial \boldsymbol{\sigma}}{\partial \nabla(\Delta \mathbf{w})}(\mathbf{x}) \cdot \mathbf{B}^w(\mathbf{x}) d\Omega \\ \mathbf{K}^{wu} & \equiv \frac{\partial \mathbf{R}^w}{\partial \Delta \mathbf{U}} = \int_{\Omega} [\mathbf{B}^w(\mathbf{x})]^T \cdot \frac{\partial \mathbf{m}}{\partial \Delta \mathbf{e}}(\mathbf{x}) \cdot \mathbf{B}^u(\mathbf{x}) d\Omega \\ \mathbf{K}^{ww} & \equiv \frac{\partial \mathbf{R}^w}{\partial \Delta \mathbf{W}} = \int_{\Omega} [\mathbf{B}^w(\mathbf{x})]^T \cdot \frac{\partial \mathbf{m}}{\partial \nabla(\Delta \mathbf{w})}(\mathbf{x}) \cdot \mathbf{B}^w(\mathbf{x}) d\Omega \end{cases} \quad (31)$$

where Eqs. (18)₁, (19)₁, (21)₂ and (24) have been used. The derivatives $\frac{\partial \boldsymbol{\sigma}}{\partial \Delta \mathbf{e}}$, $\frac{\partial \boldsymbol{\sigma}}{\partial \nabla(\Delta \mathbf{w})}$, $\frac{\partial \mathbf{m}}{\partial \Delta \mathbf{e}}$, $\frac{\partial \mathbf{m}}{\partial \nabla(\Delta \mathbf{w})}$ here may be evaluated in the routine performing the projection of the elastic predictor onto the yield locus.

³ This simplification is by no means necessary; one could of course evaluate the derivatives of the gradients of the $N_p^u(\mathbf{x})$ with respect to $\Delta \mathbf{U}$, generating thus a more cumbersome expression of the tangent matrix. We don't do it because neglecting a minor term in this expression just generates a small risk of slowing down the convergence of the iterative algorithm, without introducing any error in the solution provided that no simplification is made in the expression of the residue.

3.5. Accounting for a more complex expression of the elementary virtual work of external forces

It has been mentioned in Section 2.1 that in Gologanu et al.'s [8] model, the expression of the virtual power of external forces does *not* include a term proportional to the virtual strain rate. We shall nevertheless explain here how such a term, usually present in second-gradient models, could be accounted for in the numerical implementation proposed. The aim is to show that this implementation, duly completed as explained here, may potentially be used for *any* second-gradient model and not only that of Gologanu et al. [8].

We shall therefore assume here that the expression of the elementary virtual work of external forces $\delta\mathcal{W}_e^*$ includes an extra term of the form

$$\int_{\partial\Omega} \mathbf{X}(\Delta\mathbf{w}(\mathbf{x})).\delta(\Delta\mathbf{w}^*)(\mathbf{x}) dS.$$

Like the standard traction $\mathbf{T}(\mathbf{u})$ in Section 2.1, the “second-order traction” \mathbf{X} here is considered to be a given function of the strain increment $\Delta\mathbf{w}$ permitting to account for all classical types of higher order boundary conditions: (i) the case of a prescribed \mathbf{X} (when it is independent of $\Delta\mathbf{w}$); (ii) that of an elastic connection to some external body (when \mathbf{X} is a linear-affine function of $\Delta\mathbf{w}$); and (iii) that of a prescribed $\Delta\mathbf{w}$ (when the coefficient of this linear-affine function is large).

Rewriting Eq. (17) in the form

$$\Delta\mathbf{w}(\mathbf{x}) \equiv \mathbf{N}^w(\mathbf{x}).\Delta\mathbf{W}; \quad \delta(\Delta\mathbf{w}^*)(\mathbf{x}) \equiv \mathbf{N}^w(\mathbf{x}).\delta(\Delta\mathbf{W}^*)$$

where $\mathbf{N}^w(\mathbf{x})$ is a $6 \times 6N$ matrix involving the shape functions $N_p^w(\mathbf{x})$, one may re-express the integral above in the form

$$\int_{\partial\Omega} \mathbf{X}(\Delta\mathbf{w}(\mathbf{x})).\mathbf{N}^w(\mathbf{x}).\delta(\Delta\mathbf{W}^*) dS = \left(\int_{\partial\Omega} [\mathbf{N}^w(\mathbf{x})]^T . \mathbf{X}(\Delta\mathbf{w}(\mathbf{x})) dS \right) . \delta(\Delta\mathbf{W}^*).$$

Then the expression (24)₂ of the partial residue \mathbf{R}^w involves an extra term

$$- \int_{\partial\Omega} [\mathbf{N}^w(\mathbf{x})]^T . \mathbf{X}(\Delta\mathbf{w}(\mathbf{x})) dS$$

and the “partial tangent matrix” \mathbf{K}^{ww} involves an extra term

$$- \int_{\partial\Omega} [\mathbf{N}^w(\mathbf{x})]^T . \frac{\partial \mathbf{X}}{\partial \Delta\mathbf{w}}(\mathbf{x}).\mathbf{N}^w(\mathbf{x}) dS.$$

These are the sole modifications of the algorithm required. (In particular the expressions (29) and (30) of the total residue and tangent-matrix are left unchanged). The calculation of the extra terms in the expressions of \mathbf{R}^w and \mathbf{K}^{ww} are straightforward.

3.6. Programming aspects

A few comments on the programming are in order here:

- In the case of quadratic interpolation of \mathbf{u} -type variables and linear interpolation of \mathbf{w} -type ones, reduced Gaussian integration is used for the former variables and standard Gaussian integration for the latter. (This in fact means using the same Gauss points for all variables). In the case of linear interpolations of both \mathbf{u} - and \mathbf{w} -type variables, standard Gaussian integration is used. This integration scheme is not expected to raise any locking problem since materials obeying Gologanu et al.'s [8] model are plastically compressible.
- Exceptionally, the integrals appearing in the expression of the matrix \mathbf{M} resulting from Eq. (26) are carried out by placing integration points at the nodes. Nodal integration is appropriate for the integrals in question because it automatically results in a diagonal matrix in the left-hand side of system (25) on the $\Delta\mathbf{w}_q$, thus warranting its solution in the form of Eq. (26), as desired.
- In the expression (30) of the total tangent matrix \mathbf{K} , the partial matrices \mathbf{K}^{uu} , \mathbf{K}^{uw} , \mathbf{K}^{wu} , \mathbf{K}^{ww} “connect” only first neighbors, that is nodes lying in the same element. But the matrices \mathbf{M} and \mathbf{M}^T also connect first neighbors. As a consequence, the matrices $\mathbf{K}^{uw}.\mathbf{M}$ and $\mathbf{M}^T.\mathbf{K}^{wu}$ connect second neighbors, that is nodes having a common first neighbor, and the matrix $\mathbf{M}^T.\mathbf{K}^{ww}.\mathbf{M}$ connects third neighbors, that is nodes having some first neighbors which are themselves first neighbors. This means that when calculating the contribution of a given element to the matrix \mathbf{K} , a double loop on the nodes of this element is no longer sufficient; the loop must be on “neighbors of the element”. To define such neighbors, one proceeds in three steps. First, using the “direct connectivity table” providing the numbers of the nodes belonging to each element, one constructs an “inverse connectivity table” providing the numbers of the elements containing each node. Second, one constructs a “table of first neighbors of the nodes”; this is done by using the direct and inverse connectivity tables to find, for each node, the numbers of the nodes belonging to all elements containing it. Third, one constructs a “table of neighbors of

the elements”; this is done by using the direct connectivity table together with the table of first neighbors of the nodes to find, for every element, the numbers of the first neighbors of the nodes belonging to it.

Of course, the loop on “neighbors of elements” requires additional CPU time, but this disadvantage is more than compensated by the reduced size of the problem and the improved performance of the algorithm.

4. Validation of the programme: 2D simulation of circular bending of a beam

In order to assess the programme developed and compare the results to those obtained with Enakoutsu's [3]; Enakoutsu and Leblond's [5] previous implementation, we first consider the simple academic problem of plane strain circular bending of a beam made of a material obeying Gologanu et al.'s [8] model. A reference analytical solution to this problem was obtained by Enakoutsu [3], Enakoutsu and Leblond [5] for some special values of the model parameters.

Fig. 1 depicts the problem schematically. A beam of rectangular cross-section, center O , thickness $2h = 10\text{mm}$, axis parallel to the direction Ox , is bent in plane strain in the plane Oxy . A linear dependence of the xx -component of the strain upon the vertical coordinate y is enforced by prescribing suitable displacements on the lateral boundaries. The problem is considered within the linearized context (small displacements and strains).

The material parameters used are given in Appendix A. Since a very small value is adopted for the initial porosity f_0 but not for the microstructural distance b , we are *not* following the recommendation made finally in Section 2.7. This recommendation is pointless here because physical relevance is not the primary concern for tests aimed at assessing the correctness of a computer programme, and the choice of values made is necessary for the sake of comparison with Enakoutsu's [3], Enakoutsu and Leblond's [5] analytic solution. The choice of an almost zero porosity, which implies plastic quasi-incompressibility, is checked *a posteriori* not to generate locking problems (in the specific case considered!) by examining stress components at Gauss points and verifying that spurious variations of these components from one Gauss point to its neighbor do not occur.

Three calculations are performed:

- The first is based on Enakoutsu's [3], Enakoutsu and Leblond's [5] previous implementation, which used some penalty method to enforce coincidence of $\Delta \mathbf{w}$ and $\Delta \mathbf{e}$, coupled with a quadratic interpolation of both \mathbf{u} - and \mathbf{w} -type variables. In this case the mesh has 10 elements in the direction y .
- The second calculation is based on the present implementation, with a quadratic interpolation of \mathbf{u} -type variables and a linear interpolation of \mathbf{w} -type ones. The mesh used is identical to the previous one.
- The third calculation is also based on the present implementation, but with a linear interpolation of both \mathbf{u} - and \mathbf{w} -type variables. In that case the number of elements in the direction y is increased up to 20, in order to tentatively compensate for the well-known mediocrity of the behavior of linear elements in bending.

Figs. 2 and 3 compare theoretical results for the stress and moment components σ_{xx} , m_{xy} to those obtained in the first simulation, at a typical instant when the size $2c$ of the central elastic zone is about 0.35 times the thickness $2h$ of the beam. In the analytic solution, the stress σ_{xx} varies linearly with y in the central elastic zone, like in a standard first-gradient model, but unlike in such a model, it also slightly varies within the outer plastic zones; and the moment m_{xy} (which does not exist in a first-gradient model) is constant within the elastic zone and decreases down to zero in the plastic ones. The numerical solution does reproduce these features, but with some slight spurious oscillations, especially in the distribution of the moment.

Figs. 4 and 5 show results for the second simulation in a similar way. Numerical oscillations have disappeared, and the agreement with the analytic solution is almost perfect. The improvement obviously arises from a more logical interpolation scheme (quadratic for the displacements like before, but linear instead of quadratic for the strains).

Finally Figs. 6 and 7 show results for the third simulation. Numerical results are still excellent for the stress, but the moment is now somewhat underestimated except on the outer surfaces. This is due to use of a somewhat insufficient number of elements for the problem considered, with the linear interpolation of both \mathbf{u} - and \mathbf{w} -type variables employed here; the use of

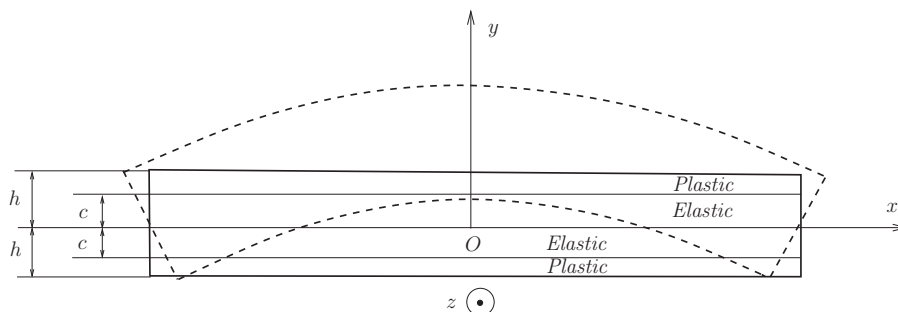


Fig. 1. Circular bending of a beam in plane strain.

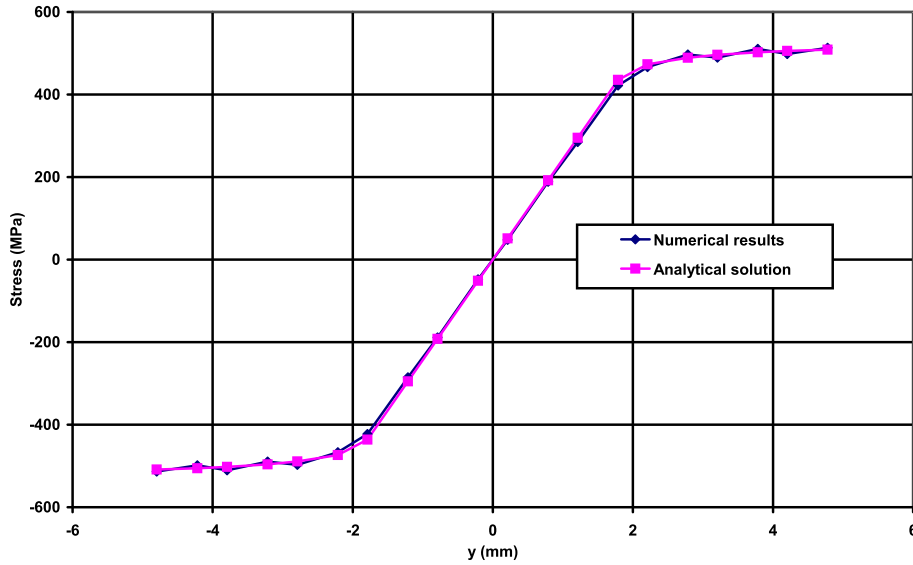


Fig. 2. Stress distribution in a beam – Previous numerical implementation, quadratic interpolations of the displacements and the strains.

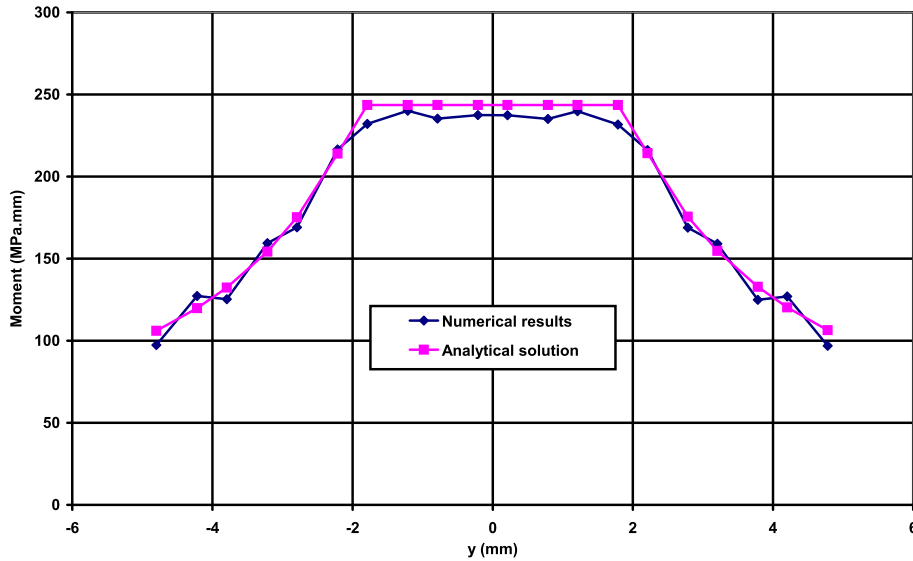


Fig. 3. Moment distribution in a beam – Previous numerical implementation, quadratic interpolations of the displacements and the strains.

more elements (not illustrated here for space reasons) is found to solve the issue. (This is an illustration of the relatively mediocre behavior of linear elements in bending).

In conclusion, for this problem of plane strain bending of a beam, the best results are obtained with the new numerical implementation, using a quadratic interpolation of \mathbf{u} -type variables and a linear interpolation of \mathbf{w} -type ones. Other elements are however in favor of a linear interpolation of both types of variables, as will be seen in the sequel.

5. Applications

5.1. Simulation of a tensile axisymmetric pre-notched and pre-cracked specimen

As a first application, we shall perform an axisymmetric simulation of Mudry's [22] fracture test of a tensile axisymmetric pre-notched and pre-cracked round bar (denoted TA30, where the number refers to the diameter) made of A508 Class 3 steel. The geometry and one of its discretizations are represented in Fig. 8. Advantage is taken of symmetry about the horizontal mid-plane to model only the upper half of the specimen, and the axis of rotational symmetry coincides with the left

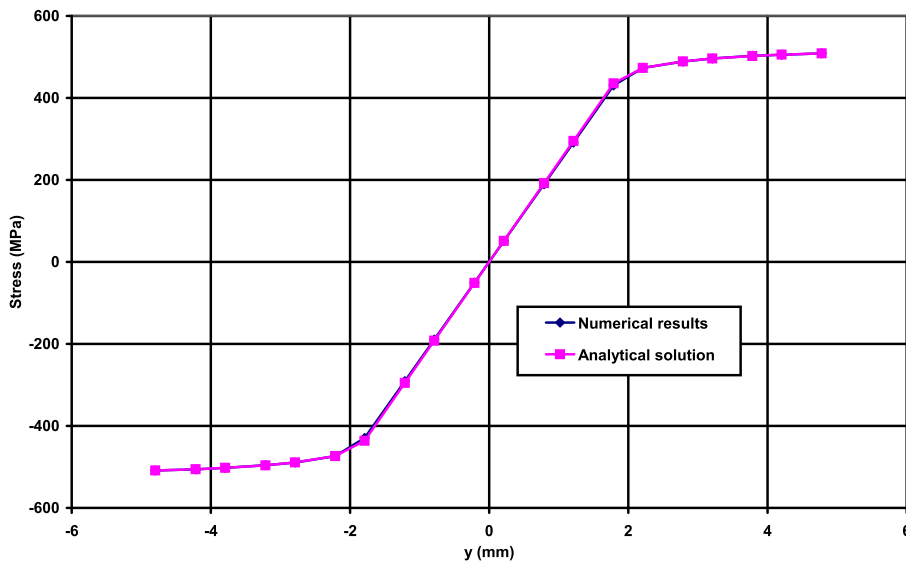


Fig. 4. Stress distribution in a beam – New numerical implementation, quadratic interpolation of the displacements, linear interpolation of the strains.

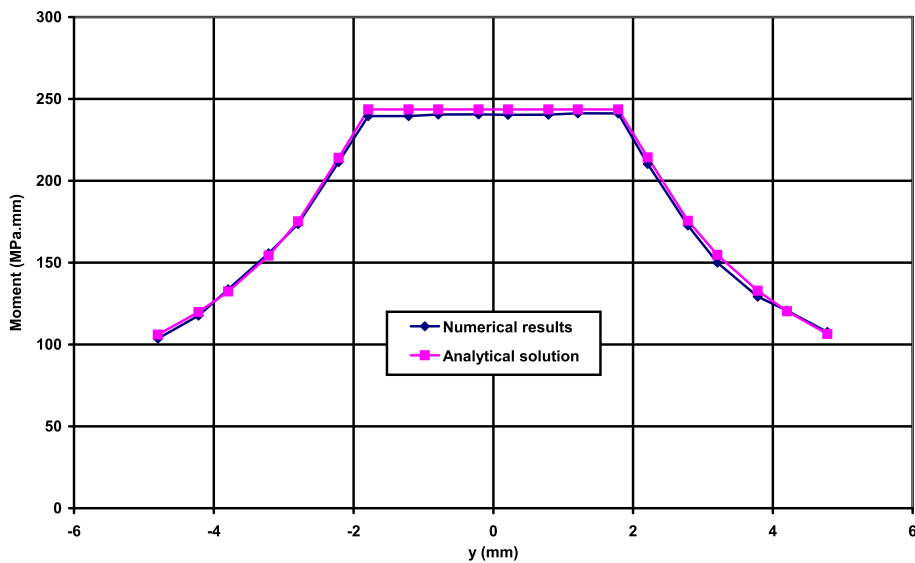


Fig. 5. Moment distribution in a beam – New numerical implementation, quadratic interpolation of the displacements, linear interpolation of the strains.

boundary of the mesh. The height and diameter of the specimen are 90 mm and 30 mm, respectively. The central notch (at the bottom of the mesh) is triangular; its opening angle and depth are 60° and 5 mm, respectively. A fatigue pre-crack of length 1.7 mm originates from the notch root. A crack develops from the tip of this pre-crack (located slightly on the left of the notch root, where the shape of the elements changes from triangular to square) and propagates toward the axis of rotational symmetry.

Two meshes are in fact used, so as to permit a study of the mesh sensitivity of the results. Figs. 9 and 10 shows enlargements of the central region of the specimen in these two meshes, which differ through the size of the square elements used in the region of the propagating crack, 0.3 mm in Fig. 9 and 0.1 mm in Fig. 10. However, strictly identical discretizations are used close to the tip of the initial fatigue pre-crack, because different discretizations would result in somewhat different geometrical representations of the initial blunting of the crack; this would induce differences in the near-peak regions of the load–displacement curves, which would have nothing to do with the mesh sensitivity arising from the softening character of the constitutive model and interfere with its study.

The number of meshes used is limited to two for the following reasons: (i) the minimum element size in both meshes is already notably smaller than the value of the microstructural distance used (see below), so that there would be no point in

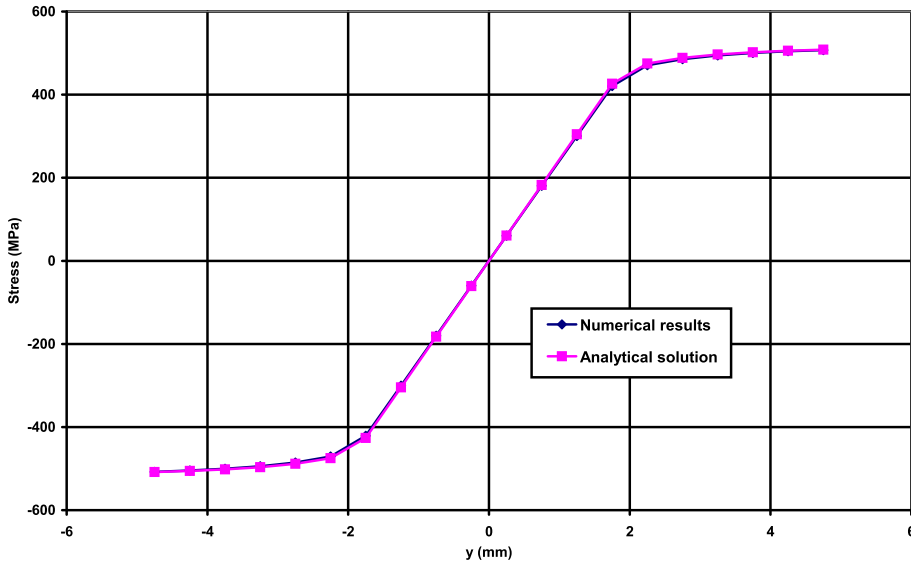


Fig. 6. Stress distribution in a beam – New numerical implementation, linear interpolations of the displacements and the strains.

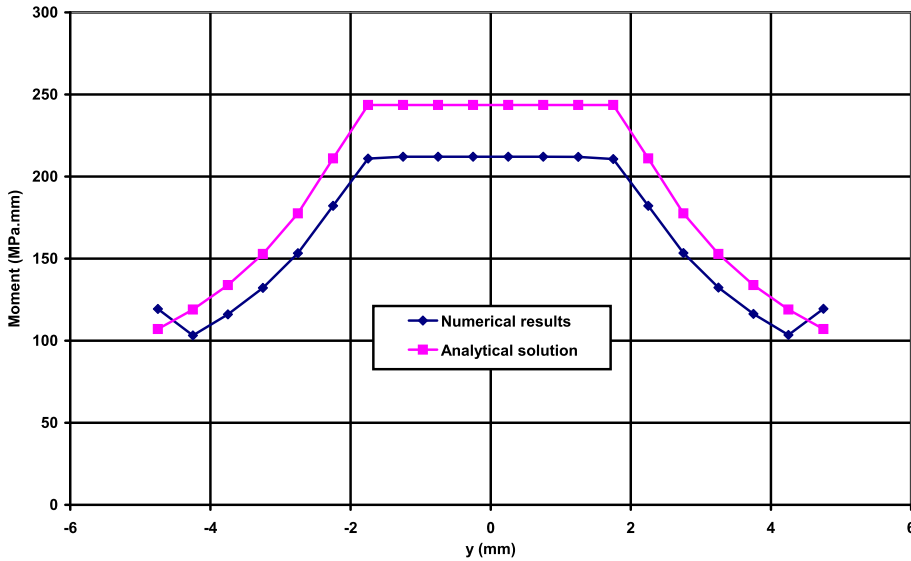


Fig. 7. Moment distribution in a beam – New numerical implementation, linear interpolations of the displacements and the strains.

decreasing it further; (ii) the issue of mesh sensitivity for the model considered has already been extensively studied by Enakoutsa [3], Enakoutsa and Leblond [5].

The values of the material parameters, not including those pertaining to coalescence of voids, are given in Appendix B. All these parameters are identical to those used in Enakoutsa's [3], Enakoutsa and Leblond's [5] previous study of the same problem, based on their earlier implementation of Gologanu et al.'s [8] model. In contrast, various values of the coalescence parameters f_c (critical porosity) and δ ("accelerating factor"), differing from those considered by Enakoutsa [3], Enakoutsa and Leblond [3,5], will be used.

Fig. 11 shows the experimental load–displacement curve (in dark blue) together with various numerical ones:

- The yellow and green⁴ curves have been obtained with the same coalescence parameters, $f_c = 0.08$ and $\delta = 4$, using the two meshes shown in Figs. 9 and 10. The purpose here was not to faithfully reproduce the experimental curve but simply to examine the influence of the mesh. It can be observed that the curves are very close, showing that the influence of the

⁴ For interpretation of color in Figs. 9–11, the reader is referred to the web version of this article.

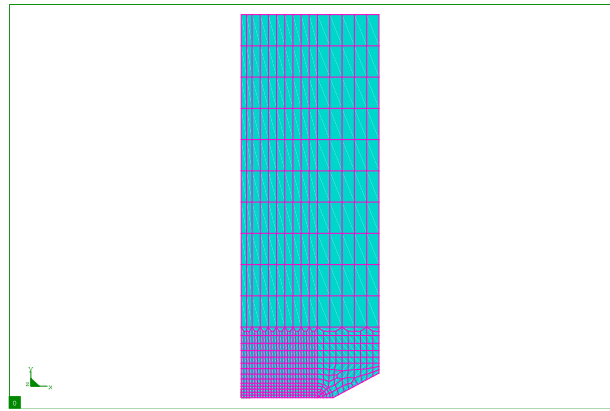


Fig. 8. General mesh of the TA30 specimen – Minimum element size 300 microns.

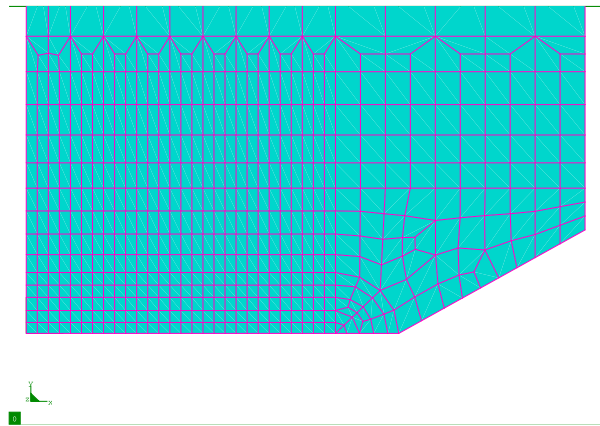


Fig. 9. Zoom of the mesh of the TA30 specimen – Minimum element size 300 microns.

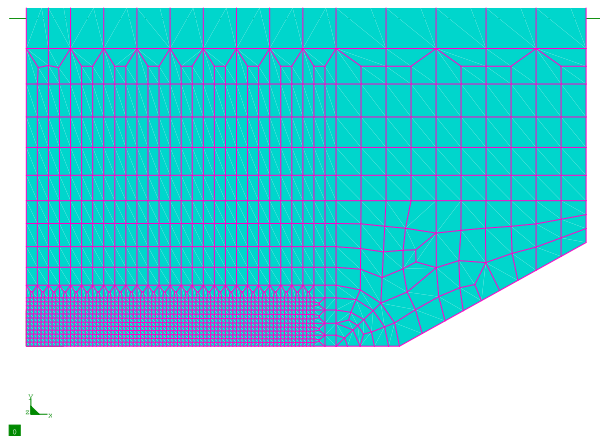


Fig. 10. Zoom of the mesh of the TA30 specimen – Minimum element size 100 microns.

discretization is minimal. (Results obtained with Gurson's standard first-gradient model would exhibit a much larger mesh sensitivity in the descending portion of the curve; the issue of mesh sensitivity with Gurson's model has been studied in detail by Tvergaard and Needleman [21]).

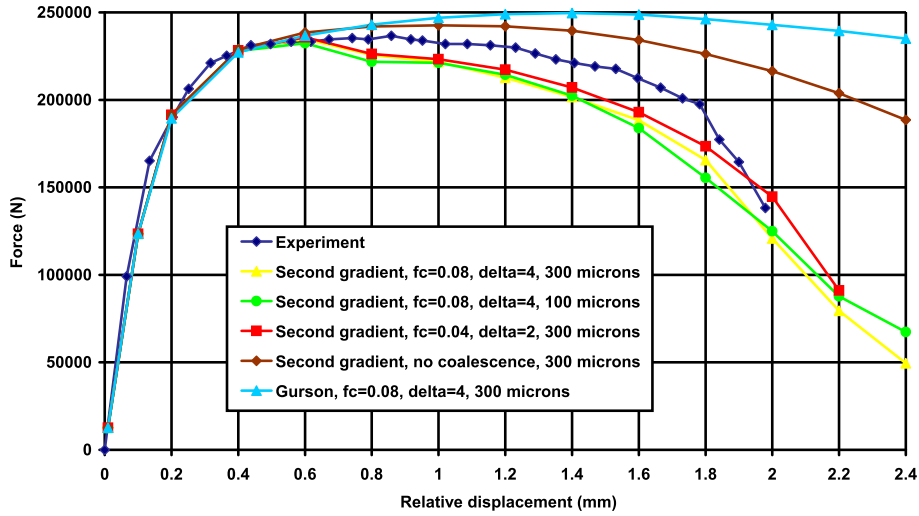


Fig. 11. Comparison of experimental and computed load–displacement curves of the TA30 specimen.

- The red curve has been obtained with the mesh shown in Fig. 9 and the parameters $f_c = 0.04$ and $\delta = 2$. Although it would probably be possible to bring it closer to the experimental one through finer adjustment of the coalescence parameters, the agreement between the two is quite acceptable, especially in view of the inherently imperfect reproducibility of experimental results. This result is remarkable in view of the qualitative compatibility of the value of f_c used with the theoretical ones, of the order of a few percent, obtained by various authors through micromechanical finite element simulations of representative porous cells, see the pioneering work of Koplik and Needleman [12] and its many successors. Such a result could never be obtained with Gurson's standard model, which was always observed to necessitate much smaller, and unrealistic values of f_c to warrant satisfactory reproduction of experimental load–displacement curves of cracked specimens.⁵
- The brown curve has been obtained with the same mesh but coalescence has been suppressed here by adopting a high value for f_c (or equivalently a unity value for δ). The large discrepancy with the experimental curve, especially in its descending portion, illustrates the necessity of accounting for coalescence to satisfactorily reproduce the test; this shows that the agreement just reported, obtained with a realistic value of f_c , is not just fortuitous.
- Finally the light blue curve has been obtained with the same mesh and coalescence parameters as the yellow one, but using Gurson's first-gradient model instead of Gologanu et al.'s [8] second-gradient extension. The much-too-modest decrease of the load illustrates the incapacity of Gurson's model to reproduce experimental results for such high values of f_c , and the necessity of using much lower, unrealistic values.

Figs. 12 and 13 permit to better appreciate the influence of the mesh. They represent the deformed geometry (without any magnification of the displacements) obtained in the two calculations represented by the yellow and green curves in Fig. 11, at time $t = 1$ s, corresponding to a relative displacement of 2 mm. The initial undeformed mesh is also shown in the background for reference. The two deformed geometries may be observed to be virtually identical. (A rather pathological distortion of elements may be observed in the region of the tip of the fatigue pre-crack in Fig. 13 for the mesh with a minimum element size of 0.1 mm; but this is unimportant since the elements located in this region are already completely destroyed).

An additional remark is also in order here about the boundary conditions on the horizontal plane of symmetry at the bottom of the mesh. For the second-gradient model considered, the kinematic conditions to be imposed on this plane because of symmetry are a zero normal velocity and a zero shear strain rate (other components of the velocity and the strain rate remaining free). However, since the numerical algorithm has been implemented for a simplified expression of the virtual power of external forces not allowing for possible kinematic conditions on the strain rate (see Sections 2.1 and 3.5 for a discussion of this topic), calculations have been performed by imposing only a zero normal velocity and letting the shear strain rate free. But Figs. 12 and 13 show that doing so has not generated any error, since the shear strain may be observed to be zero anyway along the plane of symmetry, as desired (except near the tip of the fatigue pre-crack but this is unimportant since the material is broken there).

⁵ These observations clearly mean that the transition from Gurson's standard first-gradient model to Gologanu et al.'s [8] second-gradient extension generates important differences in predicted load–displacement curves of cracked specimen; a similar phenomenon was observed by Enakoutsu et al. [4] when studying the impact of Leblond et al.'s [13] proposed introduction of a nonlocal evolution equation of the porosity into Gurson's model. The implication is that when assessing nonlocal extensions of local models, agreement of experimental and theoretical load–displacement curves should not be taken for granted but be carefully verified.

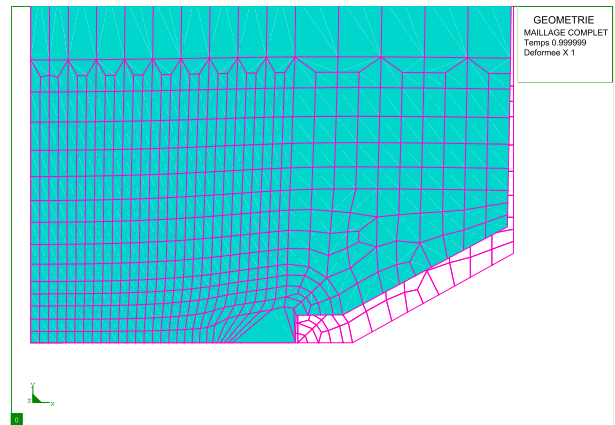


Fig. 12. Deformed mesh of the TA30 specimen at time $t = 1$ s – Minimum initial element size 300 microns.

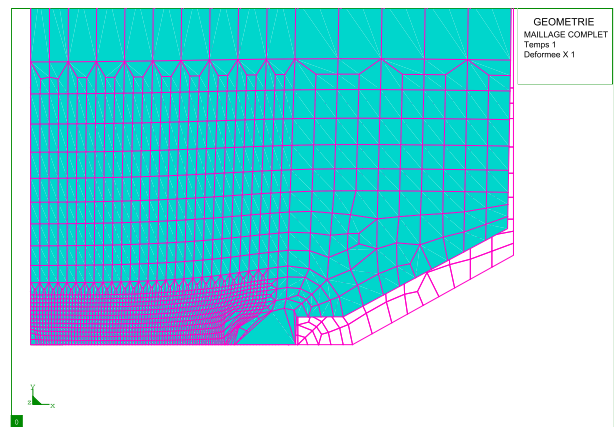


Fig. 13. Deformed mesh of the TA30 specimen at time $t = 1$ s – Minimum initial element size 100 microns.

Fig. 14 shows the distribution of the porosity on the deformed configuration of the specimen obtained in the calculation represented by the green curve in Fig. 11, in the central region of the specimen and at the last instant of the calculation ($t = 1.2$) s.⁶ Interestingly, in addition to the primary zone of high porosity originating on the right from the tip of the fatigue pre-crack, a secondary zone has made its appearance on the left, near the axis of rotational symmetry. It is thus clear that the crack initially develops from the tip of the pre-crack, but that a second crack initiates on the axis at some stage, because of the high triaxiality prevailing there.

Fig. 15 displays the distribution of the opening stress (parallel to the axis of rotational symmetry) corresponding to the porosity distribution shown in Fig. 14. One clearly sees that this stress is zero in these regions where the porosity and the distortion of elements are high, and maximal just ahead of the present crack tips.

A final remark is that all numerical results for the second-gradient model were obtained here using linear interpolations of both \mathbf{u} - and \mathbf{w} -type variables. Convergence of the global elastoplastic iterations did not raise any special difficulty under such conditions. In contrast, using a quadratic interpolation of \mathbf{u} -type variables and a linear interpolation of \mathbf{w} -type ones, it revealed impossible to pursue the calculations much beyond the maximum of the load–displacement curve because the global elastoplastic iterations ceased to converge. This difficulty was very similar to that encountered with Enakoutsu's [3], Enakoutsu and Leblond's [5] implementation of the model. Detailed inspection of the deformed meshes just before the breakdown of the calculations evidenced a very severe distortion of the triangular elements located in the crack-tip region, clearly arising from the presence of nodes half-way along the edges; the type of distortion observed is represented schematically in Fig. 16. Thus the key point in the solution of the convergence issue is the elimination of the mid-side nodes. The new treatment of the extra DOF representing strains proposed here, in spite of its advantages explained above, does not play an important role in this solution.

⁶ In this figure and the next one, the quantities plotted, known initially only at Gauss points, are extrapolated to the nodes before determining their iso-contours. It has been concluded upon trial and error that this procedure leads to optimum legibility of the figures.

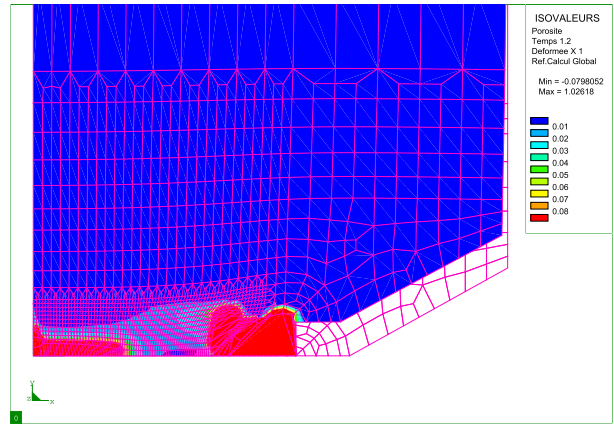


Fig. 14. Distribution of porosity on the deformed configuration of the TA30 specimen at time $t = 1.2$ s – Minimum initial element size 100 microns.

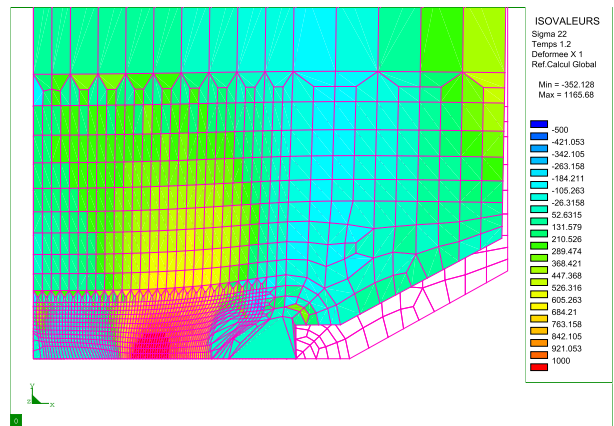


Fig. 15. Distribution of the axial stress on the deformed configuration of the TA30 specimen at time $t = 1.2$ s – Minimum initial element size 100 microns.

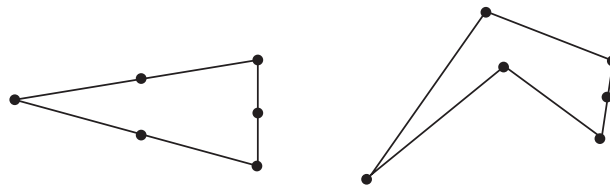


Fig. 16. Schematic shapes of a quadratic triangular element in its initial (left) and deformed (right) configurations.

5.2. Simulation of a CT specimen

As a second application, we shall perform a 2D simulation of Marie's [15] fracture test of a CT12 (where the number refers to the thickness) specimen made of SS 316L stainless steel. The discretized geometry is shown in Fig. 17. Advantage is taken of symmetry about the vertical mid-plane of the specimen to model only its right half. Its width, height and thickness are 25 mm, 25 mm and 12 mm respectively. A notch of width 2 mm and depth 85 mm originates from the top surface; this notch is rectangular near this surface, but ultimately becomes triangular, with an opening angle of 60° at the notch root. A fatigue pre-crack of length 1.34 mm originates from the notch root.

A single 2D mesh is used since the issue of mesh sensitivity has already been considered in Section 5.1 on the simulation of the TA30 specimen and also, quite comprehensively, in the works of Enakoutsu [3], Enakoutsu and Leblond [5]. The elements used in the region of the propagating crack are square with a side of 0.3 mm. All simulations are performed using a linear interpolation of both \mathbf{u} - and \mathbf{w} -type variables, since the previous study of the TA30 specimen has shown that this interpolation scheme is the solution to the convergence issue.

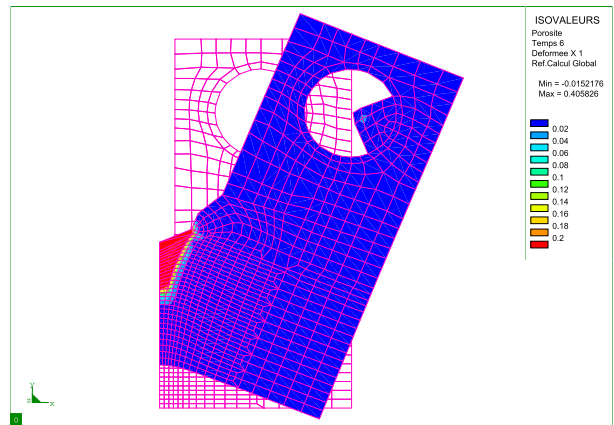


Fig. 19. Distribution of porosity on the deformed configuration of the CT specimen at time $t = 6$ s.

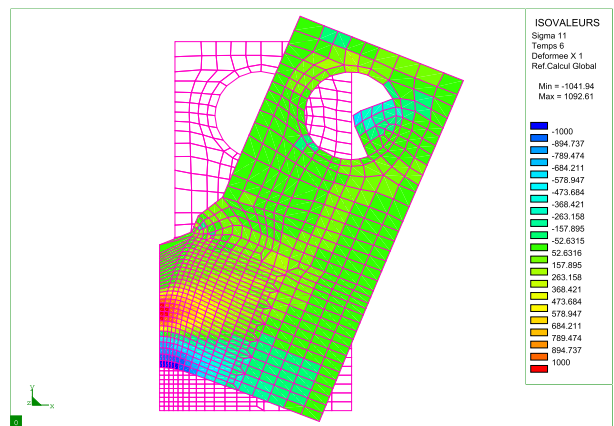


Fig. 20. Distribution of the axial stress on the deformed configuration of the CT specimen at time $t = 6$ s.

Fig. 19 shows the distribution of the porosity on the deformed configuration of the specimen (without any magnification of the displacements), at the last instant of the simulation corresponding to the red curve in Fig. 18; again, the undeformed mesh is shown in the background for reference. The important propagation of the crack and the large ensuing deformation of the specimen are quite conspicuous here.

Finally Fig. 20 shows the distribution of the opening stress (perpendicular to the crack plane) in the same simulation and at the same instant. On the vertical plane of symmetry, this stress is zero in the region of the crack, positive just ahead of the crack tip and negative beyond, as expected since the total moment of external forces must be zero.

Again, it may be observed in Fig. 20 that although the calculations have been performed by imposing only a zero normal displacement and letting the shear strain free on the vertical plane of symmetry, this has introduced no error since this shear strain may be observed to be zero there anyway, as desired (except in the destroyed region but this is unimportant).

6. Conclusion

This paper was devoted to improvements of Enakoutsu's [3], Enakoutsu and Leblond's [5] numerical implementation of Gologanu et al.'s [8] second-gradient model for ductile porous solids. The aim was to solve the two main difficulties encountered in this implementation: (i) an awkwardly large number of DOF per node, arising from the introduction of new nodal DOF representing strains; and (ii) a very problematic convergence of the global elastoplastic iterations, due to the softening character of the model. Interestingly, although the second difficulty is rather specific to the model considered, the first is not and arises for all second-gradient models; similarly, the remedy proposed to it in this paper may potentially be applied to all such models.

The major novel feature of the new implementation proposed is a procedure of elimination of the new nodal DOF representing strains, which permits to reduce the number of DOF per node to its standard value for first-gradient models, thus

solving the first difficulty mentioned above. The elimination is achieved by equating the new DOF to the strains in a weak sense; the “mass matrix” appearing in the left-hand side of the resulting system on the new DOF, analogous to those encountered in dynamic problems, may then be lumped, following the usual procedure for such problems, and inverted straightforwardly, thus permitting to express the new DOF explicitly in terms of the nodal displacements.

Also, in relation to the convergence issue, two different interpolation and integration schemes are proposed: (i) quadratic interpolation of displacements and reduced Gaussian integration of associated quantities, versus linear interpolation of strains and standard Gaussian integration of associated quantities; and (ii) linear interpolations of both displacements and strains and standard Gaussian integration of all quantities.

A 2D simulation of the academic problem of plane strain bending of a beam obeying Gologanu et al.’s [8] constitutive law, for which an analytic solution is available for some special values of the material parameters (Enakoutsa [3], Enakoutsa and Leblond [5]), has evidenced the correctness of the programme developed.

Finally, numerical simulations of an axisymmetric tensile pre-notched and pre-cracked specimen made of some low-alloy steel have evidenced several interesting features:

- The replacement of Gurson’s [9] standard first-gradient model by Gologanu et al.’s [8] second-gradient extension does lead to numerical results which are no longer mesh-dependent.
- The convergence issue may be solved through use of identical linear interpolations of all nodal variables.
- A good agreement of experimental and predicted load–displacement curves may be obtained using reasonable values of the “critical porosity” governing the onset of coalescence of voids, compatible with theoretical estimates resulting from micromechanical numerical simulations of elementary porous cells. Such a result could never be obtained with Gurson’s [9] model, which has always been observed to require unrealistically low values of this critical porosity to warrant satisfactory reproduction of experimental results.

These conclusions are also fully confirmed by simulations of a CT specimen made of some stainless steel.

Acknowledgments

The authors wish to express their warm thanks to the AREVA Company, and especially Drs. Stéphane Chapuliot and Philippe Gilles, for their continued moral and financial support of this work.

Appendix A. Material parameters for the simulations of Section 4

The material parameters for the simulations presented in Section 4 are as follows, where E denotes Young’s modulus, ν Poisson’s ratio, σ_0 the initial yield stress in simple tension, f_0 the initial porosity, A_I and A_{II} the constants involved in the expression (10) of the quadratic form Q^2 , and b the “microstructural distance”:

E (MPa)	ν	σ_0 (MPa)	Hardening law	f_0	A_I	A_{II}	b (mm)
203,000	0.499	450	Ideal plasticity	10^{-6}	0	5	1

The values of ν , f_0 , A_I , A_{II} chosen are those necessary for Enakoutsa’s [3], Enakoutsa and Leblond’s [5] analytic solution to be applicable.

Appendix B. Material parameters for the simulations of Section 5.1

The material parameters for the simulations presented in Section 5.1 are as follows, using the same notations as above plus the symbol q representing Tvergaard’s [19] parameter:

E (MPa)	ν	σ_0 (MPa)	Hardening law	q	f_0	A_I	A_{II}	b (mm)
203,000	0.3	450	See below	1.47	0.00016	0.194	6.108	0.55

Equivalent plastic strain	0	0.01	0.02	0.03	0.04	0.05	0.06	0.07
Yield stress (MPa)	450.0	482.2	516.7	546.4	569.1	587.0	600.5	611.1

0.08	0.09	0.1	0.15	0.2	0.25	0.3	0.35	0.4	0.45
620.3	627.7	633.5	659.3	678.0	693.0	705.8	716.6	725.6	734.6

0.5	0.55	0.6	0.65	0.7	0.75	0.8	0.85	0.9	0.95
742.5	749.5	755.9	761.9	767.4	772.8	777.8	782.4	787.3	791.3

Appendix C. Material parameters for the simulations of Section 5.2

E (MPa)	ν	σ_0 (MPa)	Hardening law	q	f_0	A_I	A_{II}	b (mm)
203,000	0.3	165.3	See below	1.47	0.0008	0.194	6.108	0.5

Equivalent plastic strain	0	0.00006	0.00019	0.00122	0.00327	0.01378
Yield stress (MPa)	165.3	185.3	195.3	225.4	245.9	284

0.02419	0.05376	0.09315	0.12482	0.15553	0.18534
307.4	364.1	429.3	477.2	521.4	561.4

0.21433	0.24245	0.28326	0.39584	0.49527	0.64452
597.8	631.6	676.6	784.3	866.1	973.4

0.74407	0.89346	0.94326	0.99308	1.3904	2
1037.4	1125.1	1152.5	1179.1	1369.2	1600

References

- [1] A. Brosse, Modélisation de déchirure ductile dans un tuyau inox – Calage des paramètres de Wilkins, ESI France Internal, Report F/LE/09/042/D/BPE (in French), 2009.
- [2] R. Chambon, D. Caillerie, N. El Hassan, One-dimensional localisation studied with a second grade model, *Eur. J. Mech. A/Solids* 17 (1998) 637–656.
- [3] K. Enakoutsa, Modèles non-locaux en rupture ductile des métaux, Ph.D. Thesis, Université Pierre et Marie Curie (Paris VI) (in French), 2007.
- [4] K. Enakoutsa, J.B. Leblond, G. Perrin, Numerical implementation and assessment of a phenomenological nonlocal model of ductile rupture, *Comput. Methods Appl. Mech. Engrg.* 196 (2007) 1946–1957.
- [5] K. Enakoutsa, J.B. Leblond, Numerical implementation and assessment of the GLPD micromorphic model of ductile rupture, *Eur. J. Mech. A/Solids* 28 (2009) 445–460.
- [6] R. Fernandes, C. Chavant, R. Chambon, A simplified second gradient model for dilatant materials: theory and numerical implementation, *Int. J. Solids Struct.* 45 (2008) 5289–5307.
- [7] S. Forest, Mechanics of generalized continua: construction by homogenization, *J. Phys. IV* 8 (1998), Pr4-39–Pr4-48.
- [8] M. Gologanu, J.B. Leblond, G. Perrin, J. Devaux, Recent extensions of Gurson's model for porous ductile metals, in: P. Suquet (Ed.), *Continuum Micromechanics, CISM Courses and Lectures*, vol. 377, Springer, 1997, pp. 61–130.

- [9] A.L. Gurson, Continuum theory of ductile rupture by void nucleation and growth: Part I – yield criteria and flow rules for porous ductile media, *ASME J. Engrg. Mater. Technol.* 99 (1977) 2–15.
- [10] R. Hill, The essential structure of constitutive laws for metal composites and polycrystals, *J. Mech. Phys. Solids* 15 (1967) 79–95.
- [11] T. Hughes, *The Finite Element Method: Linear Static and Dynamic Finite Element Analysis*, Dover Publications, 2000.
- [12] J. Koplik, A. Needleman, Void growth and coalescence in porous plastic solids, *Int. J. Solids Struct.* 24 (1988) 835–853.
- [13] J.B. Leblond, G. Perrin, J. Devaux, Bifurcation effects in ductile metals with nonlocal damage, *ASME J. Appl. Mech.* 61 (1994) 236–242.
- [14] J. Mandel, Contribution théorique à l'étude de l'écrouissage et des lois d'écoulement plastique, in: *Proceedings of the 11th International Congress on Applied Mechanics*, Springer, 1964, pp. 502–509 (in French).
- [15] S. Marie, Méthodes de prédiction de grandes déchirures: données expérimentales nécessaires aux modélisations, CEA Internal, Report SEMT/LISN/RT/00-020 (in French), 2000.
- [16] T. Matsushima, R. Chambon, D. Caillerie, Second gradient models as a particular case of microstructured models: a large strain finite element analysis, *Comptes-Rendus Acad. Sci. Paris Série IIb* 328 (2000) 179–186.
- [17] T. Matsushima, R. Chambon, D. Caillerie, Large strain finite element analysis of a local second-gradient model: application to localization, *Int. J. Numer. Methods Engrg.* 54 (2002) 499–521.
- [18] J. Shu, W. King, N. Fleck, Finite elements for materials with strain gradient effects, *Int. J. Numer. Methods Engrg.* 44 (1999) 373–391.
- [19] V. Tvergaard, Influence of voids on shear band instabilities under plane strain conditions, *Int. J. Fract.* 17 (1981) 389–407.
- [20] V. Tvergaard, A. Needleman, Analysis of cup-cone fracture in a round tensile bar, *Acta Metall.* 32 (1984) 157–169.
- [21] V. Tvergaard, A. Needleman, Effects of nonlocal damage in porous plastic solids, *Int. J. Solids Struct.* 32 (1995) 1063–1077.
- [22] G. Rousselier, F. Mudry, Etude de la rupture ductile de l'acier faiblement allié en Mn-Ni-Mo pour cuves de réacteurs à eau ordinaire sous pression, approvisionné sous la forme d'une débouchure de tubulure. Résultats du programme expérimental, EdF Centre des Renardières Internal Report HT/PV D529 MAT/T43 (in French), 1980.
- [23] A. Zervos, P. Papanastasiou, I. Vardoulakis, A finite element displacement formulation for gradient elastoplasticity, *Int. J. Numer. Methods Engrg.* 50 (2001) 1369–1388.